Letters

Decoupled State-Plane Analysis of Series–Series Compensated Bidirectional IPT Systems

Bo Xue, *Student Member, IEEE*, Liang Wang, *Graduate Student Member, IEEE*, Peng Zhao, *Member, IEEE*, Minfan Fu, *Senior Member, IEEE*, Junrui Liang, *Senior Member, IEEE*, and Haoyu Wang, *Senior Member, IEEE*

***Abstract*—In series–series compensated bidirectional inductive power transfer systems, the resonant currents are cross coupled due to the influence of multiresonant elements. This makes it difficult to analyze the system behavior using conventional state-plane analysis (SPA) method. To address this challenge, a novel decoupled SPA approach is proposed. It establishes two decoupled equivalent circuits and corresponding state-plane trajectories by decoupling the coupling coil model. Thus, resonant voltages and currents in switching instants can be derived. In addition, the zero-voltage-switching (ZVS) range with different phase shifts and frequency ratios can be determined, and the rms currents of coils can be analyzed quantitatively. To validate the proposed model, a 400-W-rated laboratory prototype is designed and tested. The experimental results align well with the theoretical predictions, and confirm the ZVS among all MOSFETs. The proposed method is universal and can be used to analyze other compensation networks.**

***Index Terms*—Bidirectional, inductive power transfer (IPT), state-plane analysis (SPA), zero-voltage switching (ZVS).**

NOMENCLATURE

SPA	State-plane analysis.
SRC-P	P-type series resonant converter.
SRC-N	N-type series resonant converter.
X	Model type, $\mathrm{X} \in \{\mathrm{P}, \mathrm{N}\}$.
i	Operation modes, $i \in \{1, 2, 3, 4\}$.
L, γ	Characteristic inductance and inductance ratio.
f_n	Normalized switching frequency.
g	Voltage gain.
k_φ	Phase shift direction.
$\mathbf{R}, \mathbf{C}$	Inductance and capacitance matrices.
$\mathbf{k_i}, \mathbf{k_v}$	Linear transformation matrices.
$\mathbf{L_D}, \mathbf{C_D}$	Decoupled inductance and capacitance matrices.
$L_\mathrm{X}, C_\mathrm{X}$	Equivalent inductance and capacitance.
ω_X	Angular frequency of X-type model.
$V_{i\mathrm{X}}, \alpha_{i\mathrm{X}}$	Centers and angles of the trajectory arcs in Fig. 4.
$J_{i\mathrm{X}}$	Normalized equivalent inductor current.
$M_{i\mathrm{X}}$	Normalized equivalent capacitor voltage.
i_{S1}, i_{S5}	Turn-ON currents of S_1 and S_5.
P_o	Output power.
$I_{\mathrm{rms}1,2}$	RMS currents of TX and RX coils.

Manuscript received 1 August 2023; revised 4 September 2023; accepted 25 September 2023. Date of publication 2 October 2023; date of current version 6 December 2023. This work was supported in part by the National Natural Science Foundation of China under Grant 52077140 and in part by the Shanghai Rising Star Program under Grant 20QA1406700. *(Corresponding author: Haoyu Wang.)*

Bo Xue is with the Power Electronics and Renewable Energies Laboratory, School of Information Science and Technology, Shanghai Tech University, Shanghai 201210, China, also with the Shanghai Institute of Microsystem and Information Technology, Chinese Academy of Sciences, Shanghai 200050, China, and also with the University of Chinese Academy of Sciences, Beijing 100049, China (e-mail: xuebo@shanghaitech.edu.cn).

Liang Wang, Peng Zhao, Minfan Fu, Junrui Liang, and Haoyu Wang are with the Center for Intelligent Power and Energy Systems, School of Information Science and Technology, Shanghai Tech University, Shanghai 201210, China (e-mail: wangliang1@shanghaitech.edu.cn; zhaopeng@shanghaitech.edu.cn; fumf@shanghaitech.edu.cn; liangjr@shanghaitech.edu.cn; wanghy@shanghaitech.edu.cn).

Color versions of one or more figures in this article are available at https://doi.org/10.1109/TPEL.2023.3321316.

Digital Object Identifier 10.1109/TPEL.2023.3321316

I. INTRODUCTION

INDUCTIVE power transfer (IPT) technology is booming in various applications due to its flexibility, convenience, and safety [1]. The modeling of IPT systems provides critical guidance to the optimal design of IPT modules [2].

First harmonic approximation (FHA) is a widely used modeling method to analyze various resonant topologies due to its simplicity. However, FHA model considers only the first harmonic component while ignoring all higher harmonics. This limits its accuracy, especially under high distortion, which often occur during light load conditions [3], [4].

Alternatively, time-domain analysis has been investigated to improve the modeling accuracy [5], [6]. However, most time-domain methods rely on numerical solutions, making it challenging to obtain the analytical expressions of resonant currents and voltages. In [7], a differential equation-based modeling and analysis method is proposed for strongly coupled IPT systems. Nevertheless, solving the coefficients in this approach is overly complex. In [8], a harmonics-based time-domain model for bidirectional IPT systems is proposed to analyze the zero-voltage-switching (ZVS) range. However, this model relies on harmonic analysis, which is inaccurate when the coil currents are highly distorted.

State-plane analysis (SPA) is a graphical and geometrical method used in the design and analysis of resonant converters [9], [10]. However, it is challenging to implement

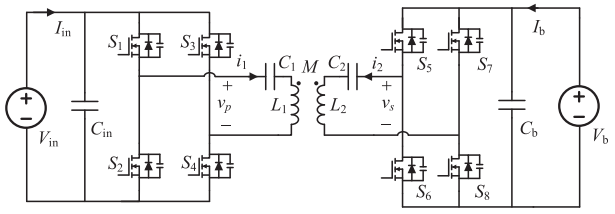

Fig. 1. Schematic of SS compensated bidirectional IPT system.

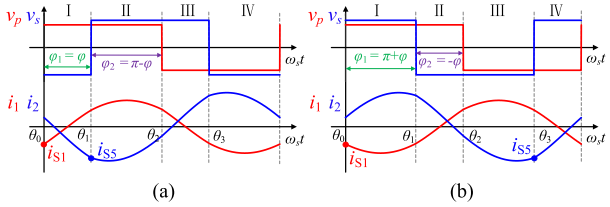

Fig. 2. Critical steady-state waveforms. (a) $\varphi \geq 0 (k_\varphi = 1)$. (b) $\varphi < 0$ $(k_\varphi = -1)$.

SPA when dealing with systems with more than three resonant elements: the state trajectories cannot be shown in a plane due to the coupling between multiresonant components. In [11], a generalized SPA approach is proposed for bidirectional CLLC resonant converters. Nevertheless, the coefficients are difficult to solve and the rms currents cannot be obtained.

In this letter, a novel decoupled SPA method is proposed for series–series (SS) compensated bidirectional IPT systems. Through a series of matrix calculations, we successfully decoupled the coupling coil model into two equivalent circuits, which enables the establishment of corresponding state-plane trajectories. This approach allows us to accurately predict the ZVS range and rms current of the coupling coils under various operating conditions. Moreover, the proposed method has strong versatility and can provide insights for the analysis and design of other high-order compensation networks. The experimental results show that the proposed model exhibits high accuracy at all load conditions.

II. Modeling and Derivation

The schematic of SS compensated bidirectional IPT system is plotted in Fig. 1, where $V_{\rm in}$ is the dc-link voltage, $V_{\rm b}$ is the battery voltage, and v_p and v_s are the voltages of inverter and rectifier, respectively. L_1 and L_2 are the self-inductances of transmitter (TX) and receiver (RX) coils, respectively. C_1 and C_2 are the corresponding compensation capacitances. M is the mutual inductance between the TX and RX coils. $M = k\sqrt{L_1 L_2}$, where k is the coupling coefficient.

The circuit parameters of the converter are defined as

$$\omega_0 = 2\pi f_0 = \frac{1}{\sqrt{L_1 C_1}} = \frac{1}{\sqrt{L_2 C_2}}, \quad f_n = f_s / f_0$$
$$L = \sqrt{L_1 L_2}, \quad \gamma = \sqrt{L_1 / L_2}, \quad g = V_{\rm b}/V_{\rm in} \tag{1}$$

where ω_0, f_s, and f_n are the angular resonant frequency, switching frequency, and normalized switching frequency, respectively. L, γ, and g are the characteristics inductance, characteristics inductance ratio, and voltage gain, respectively.

Fig. 2 shows the typical steady-state waveforms with different phase shifts, where φ is the phase shift between v_p and v_s. As indicated, k_φ is defined as phase shift direction. φ_1 and φ_2 are the durations of modes I and II, respectively. i_{S1} and i_{S5} are the currents when switches S_1 and S_5 are turned ON, respectively.

A. Decoupling Analysis

To simplify the analysis, the impact of dead time and the output voltage rise/drop times of the full bridge are ignored.

We take the inductor currents and capacitor voltages i_1, i_2, v_1, and v_2 as the state variables. $\mathbf{u} = [v_p(t); v_s(t)]$, $\mathbf{v} = [v_1(t); v_2(t)]$, and $\mathbf{i} = [i_1(t); i_2(t)]$ are defined as the input voltage vector, capacitor voltage vector, and current vector, respectively. The circuit model can be established as

$$\begin{cases} \mathbf{R}\mathbf{i}' + \mathbf{v} = \mathbf{u} \\ \mathbf{i} = \mathbf{C}\mathbf{v}' \end{cases} \tag{2}$$

where $\mathbf{R}$ and $\mathbf{C}$ are the inductance matrix and capacitance matrix, and are defined as

$$\mathbf{R} = \begin{bmatrix} L_1 & M \\ M & L_2 \end{bmatrix}, \ \mathbf{C} = \begin{bmatrix} C_1 & \\ & C_2 \end{bmatrix}. \tag{3}$$

However, since matrix $\mathbf{R}$ is not diagonal, the resonant currents are cross coupled. Based on matrix theory, there exists nonsingular matrices $\mathbf{P} = [\mathbf{p_1}; \mathbf{p_2}]$ and $\mathbf{\Lambda} = \mathrm{diag}\{\lambda_1, \lambda_2\}$ that satisfy the following equation [6]:

$$\mathbf{RCP} = \mathbf{P\Lambda} \tag{4}$$

where λ_1, λ_2, and $\mathbf{p_1}$ and $\mathbf{p_2}$ are the eigenvalues and corresponding eigenvectors of $\mathbf{RC}$.

Using linear transformations,

$$\mathbf{i_D} = \mathbf{k_i i}, \quad \mathbf{v_D} = \mathbf{k_v v}, \quad \mathbf{u_D} = \mathbf{k_v u}$$
$$\mathbf{k_i} = \mathbf{C P^{-1} C^{-1}} = \begin{bmatrix} 1 & -1/\gamma \\ \gamma & 1 \end{bmatrix}, \mathbf{k_v} = \mathbf{P^{-1}} = \begin{bmatrix} 1 & -\gamma \\ 1/\gamma & 1 \end{bmatrix}. \tag{5}$$

The coupled state-space model in (2) can be decoupled into two distinct and mutually independent equations

$$\begin{cases} \mathbf{L_D}\mathbf{i}_\mathbf{D}' + \mathbf{v_D} = \mathbf{u_D} \\ \mathbf{i_D} = \mathbf{C_D}\mathbf{v}_\mathbf{D}' \end{cases} \tag{6}$$

where $\mathbf{L_D} = \mathbf{\Lambda C^{-1}} = \mathrm{diag}\{(1-k)L_1, (1+k)L_2\}$, and $\mathbf{C_D} = \mathbf{C}$. $\mathbf{u_D} = [u_{\rm P}; u_{\rm N}]$, $\mathbf{v_D} = [v_{\rm P}; v_{\rm N}]$, and $\mathbf{i_D} = [i_{\rm P}; i_{\rm N}]$ are the input voltage vector, voltage vector, and current vector of the decoupled model (6), respectively. Since matrices $\mathbf{L_D}$ and $\mathbf{C_D}$ are diagonal matrices, $i_{\rm P}$ and $i_{\rm N}$ are independent of each other.

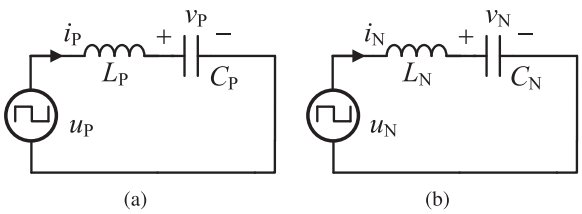

Fig. 3. Equivalent circuit. (a) SRC-P. (b) SRC-N.

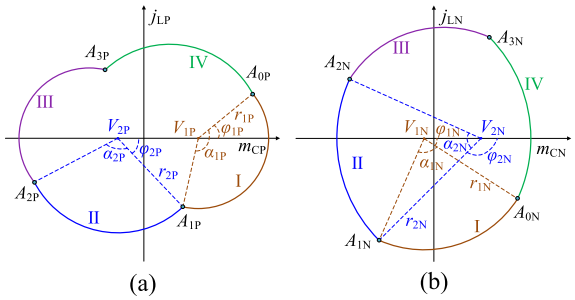

Fig. 4. Normalized state-plane trajectories of the equivalent circuits. (a) SRC-P. (b) SRC-N.

B. State-Plane Analysis

Fig. 3(a) and (b) represents the equivalent circuits described by (6), which are denoted by the P-type series resonant converter (SRC-P) and the N-type series resonant converter (SRC-N), respectively. It can be seen that the BIPT system can be modeled by two independent series resonant converters, where $L_P = (1-k)L_1, L_N = (1+k)L_2, C_P = C_1$, and $C_N = C_2$ are the corresponding equivalent inductance and capacitance. The equivalent angular frequency and characteristics impedance of SRC-P and SRC-N are defined as

$$\omega_X = 1/\sqrt{L_X C_X} = r_X \omega_0, Z_X = \omega_X L_X, X \in \{P, N\} \quad (7)$$

where $r_P = 1/\sqrt{1-k}, r_N = 1/\sqrt{1+k}$.

The equivalent voltages and currents in Fig. 3 are normalized and defined as $\mathbf{m_C} = [m_{CP}; m_{CN}]$ and $\mathbf{j_L} = [j_{LP}; j_{LN}]$

$$\mathbf{m_C} = \mathbf{V_{base}^{-1} v_D}, \quad \mathbf{j_L} = \mathbf{I_{base}^{-1} i_D} \quad (8)$$

where $\mathbf{V_{base}} = \mathrm{diag}\{V_{in}, V_b\}$ and $\mathbf{I_{base}} = \mathrm{diag}\{\frac{V_{in}}{Z_P}, \frac{V_b}{Z_N}\}$.

Fig. 4 shows the normalized state-plane trajectories of SRC-P and SRC-N. In this figure, points $A_{iP}, A_{iN}, i \in \{0,1,2,3\}$ correspond to θ_i instants of models SRC-P and SRC-N, respectively. As shown, the trajectories are symmetrical about the origin. Therefore, only modes I and II need to be analyzed. $V_{iX}, \alpha_{iX}, i \in \{1,2\}, X \in \{P, N\}$ are the centers and angles of arcs for models SRC-P and SRC-N in modes I and II, respectively.

The centers of arcs for models SRC-P and SRC-N satisfy

$$\begin{cases} V_{1P} = 1 + k_\varphi g_\gamma \\ V_{2P} = 1 - k_\varphi g_\gamma \end{cases}, \quad \begin{cases} V_{1N} = 1/g_\gamma - k_\varphi \\ V_{2N} = 1/g_\gamma + k_\varphi \end{cases} \quad (9)$$

where $g_\gamma = g\gamma$.

As shown in Fig. 4, the trajectories in mode i satisfy

$$\begin{cases} j_{iX}(\theta) = r_{iX} \sin[\varphi_{iX} - (\theta - \theta_{i-1})\omega_X/\omega_s] \\ m_{iX}(\theta) = r_{iX} \cos[\varphi_{iX} - (\theta - \theta_{i-1})\omega_X/\omega_s] + V_{iX} \end{cases} \quad (10)$$

where $\theta = \omega_s t$, and φ_{iX} and r_{iX} are the initial phase and radii of arcs. The angles of arcs α_{iX} in different modes satisfy

$$\alpha_{iX} = (\theta_i - \theta_{i-1})\omega_X/\omega_s = \varphi_i \omega_X/\omega_s. \quad (11)$$

According to (10) and (11), and Fig. 4, in mode i, the coordinates at initial state $\mathbf{A}_{(i-1)X} = [J_{(i-1)X}; M_{(i-1)X}]$ and final state $\mathbf{A}_{iX} = [J_{iX}; M_{iX}]$ satisfy the following equation:

$$\mathbf{A}_{iX} = \begin{bmatrix} \cos\alpha_{iX} & -\sin\alpha_{iX} \\ \sin\alpha_{iX} & \cos\alpha_{iX} \end{bmatrix} \mathbf{A}_{(i-1)X} + \begin{bmatrix} \sin\alpha_{iX} \\ 1-\cos\alpha_{iX} \end{bmatrix} V_{iX}. \quad (12)$$

Since the trajectories are symmetrical about the origin, $\mathbf{A}_{2X} + \mathbf{A}_{0X} = \mathbf{0}$, the solution of $\mathbf{A_{0X}}$ and $\mathbf{A_{1X}}$ can be derived as follows:

$$\mathbf{A}_{0X} = \begin{bmatrix} J_{0X} \\ M_{0X} \end{bmatrix} = \frac{1}{\cos\Phi_{X0}} \begin{bmatrix} -V_{X0}\sin\Phi_{X0} + V_{X1}\sin\Phi_{X1} \\ V_{X1}(\cos\Phi_{X0} - \cos\Phi_{X1}) \end{bmatrix}$$
$$\mathbf{A}_{1X} = \begin{bmatrix} J_{1X} \\ M_{1X} \end{bmatrix} = \frac{1}{\cos\Phi_{X0}} \begin{bmatrix} -V_{X0}\sin\Phi_{X1} + V_{X1}\sin\Phi_{X0} \\ V_{X0}(\cos\Phi_{X0} - \cos\Phi_{X1}) \end{bmatrix} \quad (13)$$

where

$$\begin{cases} \Phi_{X0} = \frac{\alpha_{2X}+\alpha_{1X}}{2} \\ \Phi_{X1} = \frac{\alpha_{2X}-\alpha_{1X}}{2} \end{cases}, \quad \begin{cases} V_{X0} = \frac{V_{1X}+V_{2X}}{2} \\ V_{X1} = \frac{V_{1X}-V_{2X}}{2}. \end{cases} \quad (14)$$

It should be noted that when $f_n = r_X$, Φ_{X0} is $\pi/2$, and the system is unstable.

Substitute $\mathbf{A}_{0X}$ and $\mathbf{A}_{1X}$ into (5) and (8), the turn ON currents of S_1 and S_5 are

$$\begin{cases} i_{S1} = i_1(\theta_0) = a_1 J_{0P} + b_1 J_{0N} \\ i_{S5} = k_\varphi i_2(\theta_1) = k_\varphi(a_2 J_{1P} + b_2 J_{1N}) \end{cases} \quad (15)$$

where

$$\begin{cases} a_1 = 0.5V_{in}/Z_P \\ b_1 = 0.5V_b/(\gamma Z_N) \end{cases}, \quad \begin{cases} a_2 = 0.5\gamma V_{in}/Z_P \\ b_2 = 0.5V_b/Z_N. \end{cases} \quad (16)$$

The detailed turn-ON currents are shown in as (17) shown at the bottom of the next page. To ensure ZVS for power MOSFETs, the minimum current to charge and discharge C_{oss} of two complementary MOSFETs is defined as $I_{min1} = 2V_{in}C_{oss}/t_d, I_{min2} = 2V_b C_{oss}/t_d$, the following constraints should be satisfied:

$$\begin{cases} S_{1,2,3,4} : i_{S1} < -I_{min1} \\ S_{5,6,7,8} : i_{S5} < -I_{min2}. \end{cases} \quad (18)$$

The output power P_o is

$$P_o = \frac{1}{T_s}\int_0^{T_s} v_p i_1 dt = -2f_s C_1 V_{in}^2 (M_{0P} + g_\gamma M_{0N}) \quad (19)$$

where M_{0P} and M_{0N} are the normalized equivalent capacitor voltages of SRC-P and SRC-N at θ_0 instant, respectively.

Fig. 5 shows the simulated and calculated results of i_{S1} and i_{S5} with different f_n. As shown, SPA exhibits higher accuracy than FHA method across the entire φ range.

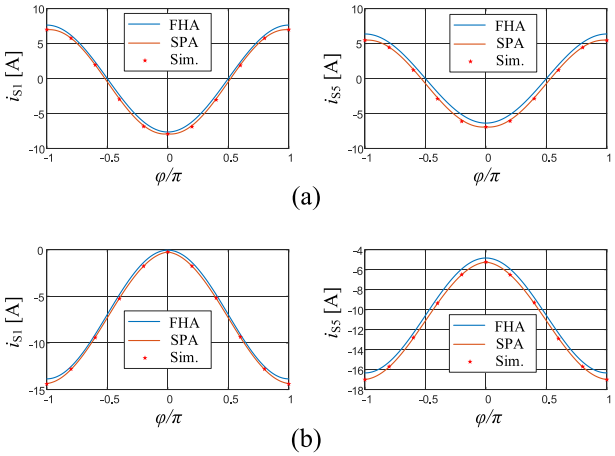

Fig. 5. Turn-ON currents of S_1 and S_5 versus φ with different f_n.(a) $f_n = 1.0$. (b) $f_n = 1.3$.

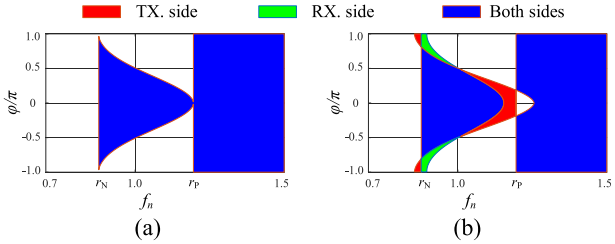

Fig. 6. ZVS range versus f_n with different g_γ. (a) $g_\gamma = 1.0$. (b) $g_\gamma = 1.2$.

The ZVS range versus f_n with different g_γ are shown in Fig. 6. As shown, the red, green, and blue areas represent the ZVS range on TX side, RX side, and both sides, respectively. The system is unstable when $f_n = r_\mathrm{X}, \mathrm{X} \in \{\mathrm{P}, \mathrm{N}\}$, which is exactly the boundary of ZVS. Different f_n correspond to different ZVS ranges. When $f_n \in [r_\mathrm{N}, r_\mathrm{P}]$, the ZVS range narrows with the increases of f_n.

The rms currents of TX and RX coils are

$$\begin{cases} I_{\mathrm{rms1}} = \sqrt{\frac{1}{\pi}\sum_{i=1}^{2}\int_{\theta_{i-1}}^{\theta_i}(a_1 j_{i\mathrm{P}} + b_1 j_{i\mathrm{N}})^2 d\theta} \\ I_{\mathrm{rms2}} = \sqrt{\frac{1}{\pi}\sum_{i=1}^{2}\int_{\theta_{i-1}}^{\theta_i}(a_2 j_{i\mathrm{P}} + b_2 j_{i\mathrm{N}})^2 d\theta}. \end{cases} \tag{20}$$

According to (20), the rms current can be solved separately in two parts. By solving (20), the following equation can be obtained:

$$\begin{cases} I_{\mathrm{rms1}} = \sqrt{k_a a_1^2 + 2k_{ab}a_1 b_1 + k_b b_1^2} \\ I_{\mathrm{rms2}} = \sqrt{k_a a_2^2 + 2k_{ab}a_2 b_2 + k_b b_2^2} \end{cases} \tag{21}$$

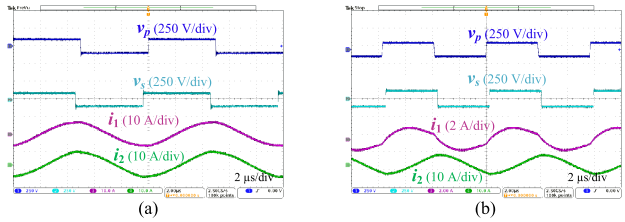

Fig. 7. Experimental steady-state waveforms with $P_o = 100$ W for different f_n and g. (a) $f_n = 1.0, g = 1.0$. (b) $f_n = 1.3, g = 1.2$.

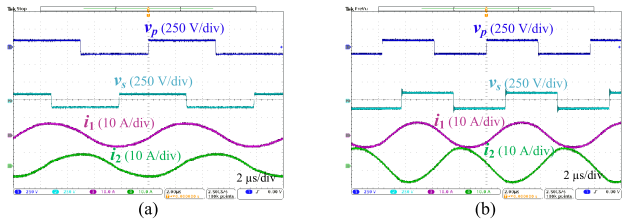

Fig. 8. Experimental steady-state waveforms with $P_o = 400$ W for different f_n and g. (a) $f_n = 1.0, g = 1.0$. (b) $f_n = 1.3, g = 1.2$.

where k_a, k_b, and k_{ab} satisfy

$$\begin{cases} k_a = \frac{\omega_s\left[r_{1\mathrm{P}}^2\alpha_{1\mathrm{P}} + r_{2\mathrm{P}}^2\alpha_{2\mathrm{P}} + 2(J_{0\mathrm{P}} - k_\varphi g_\gamma J_{1\mathrm{P}})\right]}{2\pi\omega_\mathrm{P}} \\ k_b = \frac{\omega_s\left[r_{1\mathrm{N}}^2\alpha_{1\mathrm{N}} + r_{2\mathrm{N}}^2\alpha_{2\mathrm{N}} + 2(J_{0\mathrm{N}}/g_\gamma + k_\varphi J_{1\mathrm{N}})\right]}{2\pi\omega_\mathrm{N}} \\ k_{ab} = \frac{\omega_s[2\omega_\mathrm{P}(J_{0\mathrm{N}} - k_\varphi g_\gamma J_{1\mathrm{N}}) - 2\omega_\mathrm{N}(J_{0\mathrm{P}}/g_\gamma + k_\varphi J_{1\mathrm{P}})]}{\pi(\omega_\mathrm{P}^2 - \omega_\mathrm{N}^2)} \end{cases} \tag{22}$$

and the radii of the arcs $r_{1\mathrm{P}}, r_{2\mathrm{P}}, r_{1\mathrm{N}}$, and $r_{2\mathrm{N}}$ satisfy

$$r_{i\mathrm{X}} = \sqrt{J_{(i-1)\mathrm{X}}^2 + (M_{(i-1)\mathrm{X}} - V_{i\mathrm{X}})^2}. \tag{23}$$

In summary, the procedures of the proposed modeling method are summarized as follows.

1) Decouple the coupling coils' model by matrices $\mathbf{k_i}$ and $\mathbf{k_v}$.
2) Establish two decoupled models and corresponding state-plane trajectories by decoupled model (6).
3) Calculate the currents and voltages of decoupled models at switch turn-ON instants $\mathbf{A}_{0\mathrm{X}}$ and $\mathbf{A}_{1\mathrm{X}}$ from (13).
4) Substitute $\mathbf{A}_{0\mathrm{X}}$ and $\mathbf{A}_{1\mathrm{X}}$ into (5) and (8) to calculate $i_{\mathrm{S1}}, i_{\mathrm{S5}}, P_o, I_{\mathrm{rms1}}$, and I_{rms2}.

III. Experimental Validation

A 400-W SS compensated BIPT system with 100 V input has been developed to validate the proposed analysis. The key parameters are: f_0 =100 kHz, $L_1 = 119.3$ μH, $L_2 = 94.1$ μH, $C_1 = 21.2$ nF, $C_2 = 26.9$ nF, and $k = 0.3$.

Figs. 7 and 8 show the steady-state waveforms with 100 and 400 W output, respectively. As shown, with the increase of output power, the corresponding phase shift φ increases. With

$$\begin{cases} i_{S1} = \frac{gV_\mathrm{in}}{2\omega_0 L}\left\{\frac{-\sin(0.5\pi r_\mathrm{P}/f_n)/g_\gamma + \sin[(0.5\pi - k_\varphi\varphi)r_\mathrm{P}/f_n]}{\cos(0.5\pi r_\mathrm{P}/f_n)} r_\mathrm{P} - \frac{\sin(0.5\pi r_\mathrm{N}/f_n)/g_\gamma + \sin[(0.5\pi - k_\varphi\varphi)r_\mathrm{N}/f_n]}{\cos(0.5\pi r_\mathrm{N}/f_n)} r_\mathrm{N}\right\} \\ i_{S5} = \frac{V_\mathrm{in}}{2\omega_0 L}\left\{\frac{-g_\gamma\sin(0.5\pi r_\mathrm{P}/f_n) + \sin[(0.5\pi - k_\varphi\varphi)r_\mathrm{P}/f_n]}{\cos(0.5\pi r_\mathrm{P}/f_n)} r_\mathrm{P} - \frac{g_\gamma\sin(0.5\pi r_\mathrm{N}/f_n) + \sin[(0.5\pi - k_\varphi\varphi)r_\mathrm{N}/f_n]}{\cos(0.5\pi r_\mathrm{N}/f_n)} r_\mathrm{N}\right\} \end{cases} \tag{17}$$

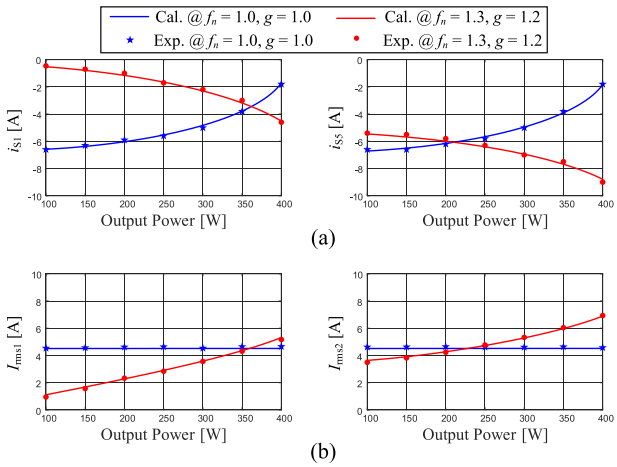

Fig. 9. Experimentally measured current values versus P_o. (a) i_{S1} and i_{S_5}. (b) I_{rms1} and I_{rms2}.

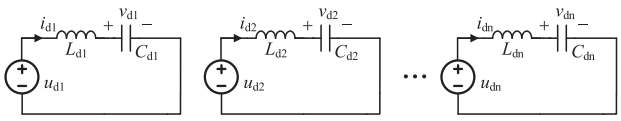

Fig. 10. Generalized decoupled equivalent series resonant circuits.

identical power transmission, the same P_o transmitted condition, v_p lags v_s in $f_n = 1.0$ and $g = 1.0$ case while leads in $f_n = 1.3$ and $g = 1.2$ case.

The turn ON currents i_{S1} and i_{S5}, and coil currents I_{rms1} and I_{rms2} versus P_o are plotted in Fig. 9. As shown, the proposed SPA are consistent with experimental results over wide load range. Fig. 9(a) shows the turn ON currents versus P_o. i_{S1} and i_{S5} are less than 0 in full-load range, which ensures ZVS turning ON of all MOSFETs. $i_{\mathrm{S1,5}}$ increases with the increase of P_o at $f_n = 1.0$ case, while decreases with the increase of P_o at $f_n = 1.3$ case. Fig. 9(b) shows the rms currents versus P_o with different f_n and g. $I_{\mathrm{rms1,2}}$ increases with the increase of P_o at $f_n = 1.3$ while stays constant at $f_n = 1.0$. This is mainly because the system operates in fully tuned mode at $f_n = 1.0$, and the rms currents of TX and RX coils are load independent.

IV. Application to Other Compensations

In fact, the proposed decoupling method applies not only to SS compensation, but also to other compensation networks.

As indicated in [6], different compensations have the same state equation form as (2), the difference is that the coefficient matrix is different. Similarly, the coupled state equation can be decoupled into (6) by using the corresponding linear transformation matrices $\mathbf{k_i}$ and $\mathbf{k_v}$. Therefore, the decoupled equivalent series resonant circuits and corresponding state-plane trajectories can be established.

Fig. 10 shows the generalized decoupled equivalent series resonant circuit, where the number of circuits n is the dimension of matrix $\mathbf{C_D}$. $L_{\mathrm{d}i}, C_{\mathrm{d}i}, i \in \{1, 2, \ldots, n\}$ are the diagonal elements of matrices $\mathbf{L_D}$ and $\mathbf{C_D}$. According to Fig. 10, the corresponding state plane can be established to solve the model. Therefore, the proposed decoupling method has strong versatility and can be applied to other compensation networks.

V. Conclusion

In this letter, we introduce a novel SPA modeling method for SS compensated BIPT systems. Using this approach, the coupling currents on both TX and RX sides are effectively decoupled into two independent components. Thus, two decoupled equivalent circuits and state-plane trajectories can be established. By leveraging ordinary differential equations and the geometric relationship of state-plane trajectories, crucial resonant currents and voltages at switch turn-ON instants can be extracted. The ZVS range and rms current of TX and RX coils can be accurately calculated. A 400-W rated prototype is designed to verify its effectiveness and feasibility. The results predicted by the proposed model align well with the experimental results. Moreover, the proposed method is universal and provides ideas for other compensation networks.

References

[1] D. Patil, M. K. McDonough, J. M. Miller, B. Fahimi, and P. T. Balsara, "Wireless power transfer for vehicular applications: Overview and challenges," *IEEE Trans. Transp. Electrif.*, vol. 4, no. 1, pp. 3–37, Mar. 2018.

[2] D. J. Thrimawithana and U. K. Madawala, "A generalized steady-state model for bidirectional IPT systems," *IEEE Trans. Power Electron.*, vol. 28, no. 10, pp. 4681–4689, Oct. 2013.

[3] Y. Liu, U. K. Madawala, R. Mai, and Z. He, "Zero-phase-angle controlled bidirectional wireless EV charging systems for large coil misalignments," *IEEE Trans. Power Electron.*, vol. 35, no. 5, pp. 5343–5353, May 2020.

[4] A. A. Mohamed, A. Berzoy, and O. A. Mohammed, "Experimental validation of comprehensive steady-state analytical model of bidirectional WPT system in EVs applications," *IEEE Trans. Veh. Technol.*, vol. 66, no. 7, pp. 5584–5594, Jul. 2017.

[5] A. Safaee and K. Woronowicz, "Time-domain analysis of voltage-driven series-series compensated inductive power transfer topology," *IEEE Trans. Power Electron.*, vol. 32, no. 7, pp. 4981–5003, Jul. 2017.

[6] B. Xue, L. Wang, M. Fu, and H. Wang, "State-space based universal time-domain model for voltage-fed bidirectional IPT systems," *IEEE Trans. Ind. Electron.*, vol. 71, no. 1, pp. 615–624, Jan. 2024.

[7] Y. Zhang, Z. Yan, T. Kan, Y. Liu, and C. C. Mi, "Modelling and analysis of the distortion of strongly-coupled wireless power transfer systems with SS and LCC-LCC compensations," *IET Power Electron.*, vol. 12, no. 6, pp. 1321–1328, Jun. 2019.

[8] X. Zhang et al., "A control strategy for efficiency optimization and wide ZVS operation range in bidirectional inductive power transfer system," *IEEE Trans. Ind. Electron.*, vol. 66, no. 8, pp. 5958–5969, Aug. 2019.

[9] D. Biadene and G. Spiazzi, "A matrix presentation of state-plane analysis for a broad class of series-resonant converters," *IEEE Trans. Power Electron.*, vol. 33, no. 12, pp. 10935–10945, Dec. 2018.

[10] W. Han and L. Corradini, "General closed-form ZVS analysis of dual-bridge series resonant DC-DC converters," *IEEE Trans. Power Electron.*, vol. 34, no. 9, pp. 9289–9302, Sep. 2019.

[11] M. Rezayati, F. Tahami, J. L. Schanen, and B. Sarrazin, "Generalized state-plane analysis of bidirectional CLLC resonant converter," *IEEE Trans. Power Electron.*, vol. 37, no. 5, pp. 5773–5785, May 2022.